NOTE

Intraoral Approach for Imaging Teeth Using the Transverse B_1 Field Components of an Occlusally Oriented Loop Coil

Djaudat Idiyatullin,[1]* Curtis A. Corum,[1] Donald R. Nixdorf,[2,3] and Michael Garwood[1]

Purpose: The signal-to-noise ratio and resolution are two competing parameters for dental MRI and are highly dependent on the radiofrequency coil configuration and performance. The purpose of this work is to describe an intraoral approach for imaging teeth with the radiofrequency coil plane oriented orthogonally to the Zeeman field to use the transverse components of the B_1 field for transmitting and receiving the NMR signal.

Methods: A single loop coil with shape and size fitted to the average adult maxillary arch was built and tested with a phantom and human subjects in vivo on a whole-body 4 T MRI scanner. Supporting Biot-Savart law simulations were performed with Matlab.

Results: In the occlusal position (in bite plane between the upper and lower teeth), the sensitive volume of the coil encompasses the most important dental structures, the teeth and their supporting structures, while uninteresting tissues containing much higher proton density (cheeks, lips, and tongue) are outside the sensitive volume. The presented images and simulated data show the advantages of using a coil in the orthogonal orientation for dental applications.

Conclusion: The transverse components of the B_1 field of a surface coil can effectively be used for imaging of teeth and associated structures. **Magn Reson Med 000:000–000, 2013. © 2013 Wiley Periodicals, Inc.**

Key words: MRI; dental imaging; RF coil; SWIFT; UTE

X-ray based imaging modalities have dominated the practice of dentistry since their invention over a century ago. Modern dentists are increasingly embracing three-dimensional techniques such as cone-beam computerized tomography, while public awareness and concern about cumulative exposure to ionizing radiation are also increasing. These factors, in combination with recent advancements in electronics and methodologies, are motivating researchers to reconsider the potential of MRI in clinical dentistry. Studies have shown how conventional MRI can be used clinically to visualize the mandibular neurovascular bundle (1,2), study pulp structure, and vitality (3–5), reveal the anatomy and pathology of the dento-alveolar region (6), detect osteomyelitis in the mandible (7), and indirectly image highly mineralized tissue through contrast produced by an MRI-visible medium (6,8–13). The potential uses of MRI in dentistry have increased with the development of methods allowing the direct imaging of densely calcified tissues of the human body, including dentin and enamel, that have low water content (i.e., low fraction of protons from which to obtain signal) and quickly decaying signal (i.e., very short T_2 relaxation times). There are at least four different and clinically applicable MRI methods for obtaining images of densely calcified dental tissues: (a) ultrashort TE (UTE) (14–17), (b) sweep imaging with Fourier transformation, SWIFT, (18–21), (c) FID-projection imaging also called BLAST, RUFIS, WASPI, or zero TE (ZTE) (22–26), and (d) combined PETRA techniques (27). These methods now make it feasible to image these tissues, but further RF coil refinement is still needed to optimize MR signal from the teeth and supporting structures.

Dental MRI has the potential to be even more informative than x-ray imaging techniques by visualizing, noninvasively and simultaneously, both hard and soft tissues in all three spatial dimensions. However, clinical MRI has yet to attain the resolution of cone-beam computerized tomography imaging, from 0.1–0.3 mm. SNR and resolution are two competing parameters for dental MRI and are highly dependent on the RF coil configuration (filling factor) and performance. To attain the needed resolution, patient motion must be highly restricted (including avoiding swallowing); this requirement can only be met when the coil positioning does not create excessive discomfort for the patient. In addition, the pulse sequence cannot use slice- or slab-selective pulses, both to preserve signal from hard tissues having ultrashort T_2 and due to the 3d radial free-induction decay acquisition strategy of the above methods. Thus, the acquired field-of-view (FOV) must include the entire sensitive volume of the RF coil to avoid signal folding onto areas of interest in the image. In terms of linear size, the resolution of an image voxel depends on the FOV and the reconstructed matrix size. To reach the

[1]Center for Magnetic Resonance Research and Department of Radiology, University of Minnesota Medical School, Minneapolis, Minnesota, USA.
[2]Division of TMD and Orofacial Pain, University of Minnesota, Minneapolis, Minnesota, USA.
[3]Department of Neurology, University of Minnesota, Minneapolis, Minnesota, USA.

Grant sponsor: NIH; Grant numbers: P41-EB015894, P41-RR008079, S10-RR023730, S10-RR027290, S10-RR008079, and R21-CA139688.

*Correspondence to: Djaudat Idiyatullin, Ph.D., Center for Magnetic Resonance Research and Department of Radiology, University of Minnesota Medical School, Minneapolis, MN. E-mail: idiat001@umn.edu

Disclosures: Drs. Idiyatullin, Corum and Garwood are entitled to sales royalties from a technology license (SWIFT) held by GE Healthcare through the University of Minnesota for products related to the research described in this paper. The University of Minnesota has a financial interest arising from a right to receive royalty income under the terms of the license agreement. This relationship has been reviewed and managed by the University of Minnesota in accordance with its conflict of interest policies.

Received 20 February 2013; revised 25 June 2013; accepted 27 June 2013
DOI 10.1002/mrm.24893
Published online 00 Month 2013 in Wiley Online Library (wileyonlinelibrary.com).

needed resolution, of ~0.3 mm, the FOV should not exceed about 80–120 mm with 256^3-384^3 matrix sizes, respectively. An increase in matrix size is a less satisfactory way to increase resolution because it also increases the required number of radial views and therefore increases scan time. Due to these constraints, standard coils such as head or neck coils fail to achieve the spatial resolution needed for practical dental applications. Hence, a coil configured to provide a limited and sculpted FOV is highly desirable to solve this problem.

A logical approach to imaging teeth might be to adopt existing surface coil designs with extra-oral placement adjacent to the area of interest (28,29). The diameter of such a receive coil should not exceed about 120 mm because it is limited by the size of the optimal FOV. The depth of the sensitive region in the axial direction, which is perpendicular to the plane of the surface coil, is limited to about the radius of the coil. To obtain an image of, for example, a right molar tooth, the coil could be positioned on the right cheek. For an average-sized patient the distance between the coil and molar teeth is about 30–50 mm, and as a result, sensitivity is significantly diminished. In addition, with the coil in this configuration, the cheek and buccal fat produce intense signals. Hence, the resulting images will contain more signals from less important tissues.

Positioning a coil intraorally, in the buccal vestibule that is between the teeth and adjacent cheek, increases both resolution and SNR (11). By sacrificing some comfort, as well as SNR, the intense signal from the cheek can be shielded out (19). However, due to an inability to position the coil in the restricted space optimally, the root tips of the teeth appear outside the sensitive volume of such coils. Normal intraoral anatomy makes it difficult to position the coil posterior enough to obtain images of the most distal teeth in the mouth, and common variations of intraoral anatomy, such as the presence of buccal tori and frena, pose additional difficulties in positioning the coil. This suggests that using the buccal vestibule approach for RF coil placement is problematic for patient comfort and limits visualization of oral structures. Accommodating all patient sizes and anatomical variations would likely require multiple types and sizes of coils as well as repeated scans in order to obtain needed images.

In most standard uses of surface coils, the plane of the coil is oriented parallel to B_0, and it is the B_1 field component in the direction of the coil axis that produces the majority of the field used for MRI. For most applications, this orientation is optimal because the sensitive volume of the coil is close to spherical and allows images within the area to be captured. Historically, even though the sensitive volume of a loop coil is approximately spherical, it is called a surface coil, because images are usually obtained from only one side of the loop.

Interestingly, the most comfortable coil position between the teeth in the occlusal plane was never seriously considered previously. This is likely due to thoughts that in this orientation the longitudinal component (normal to the plane of the coil loop) of B_1 becomes useless, because NMR signal interacts only with B_1 components directed orthogonally to B_0. Conveniently, the transverse components (in the plane of the coil loop) of B_1 produce a sensitive volume optimally suitable for imaging of the most important dental structures. Note that only a couple of prior attempts (not related to dental imaging) of orienting a surface coil orthogonally to B_0 have been reported. (30,31). We present B_1 simulations of the coil as well as images of teeth and supporting structures. These show the advantages of using a loop coil in the occlusal position for applications of interest to dentists.

METHODS

RF Coil Design

We constructed a single loop utilizing copper foil of 10 mm width (Fig. 1a). The shape and size was chosen to fit the average adult maxillary arch (with radius about 25 mm). The foil was covered with sticky foam for comfort.

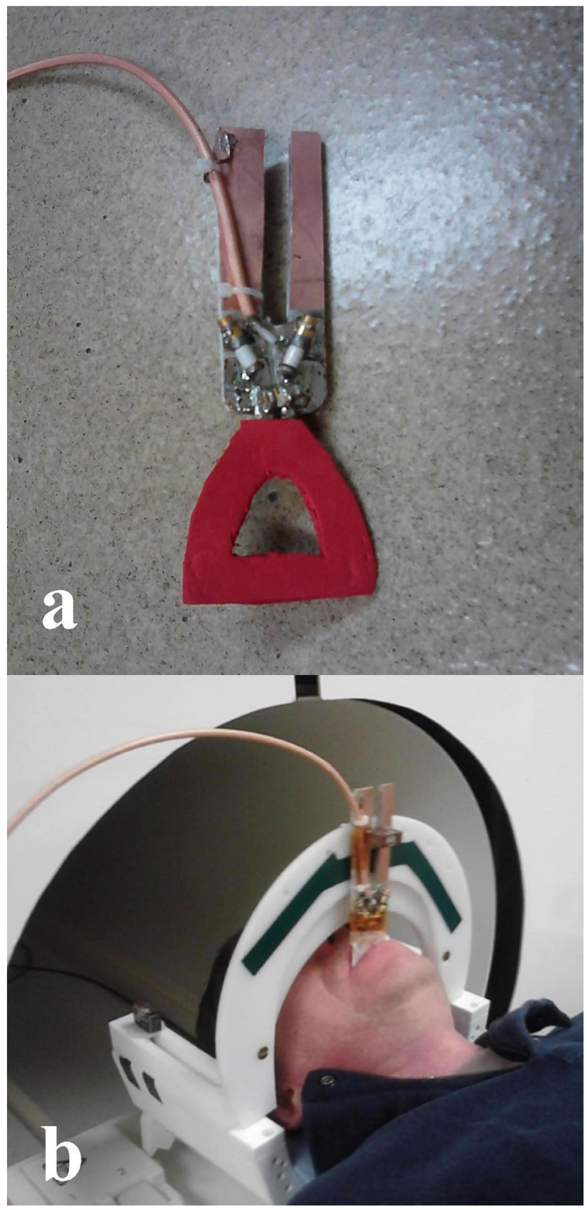

FIG. 1. Intraoral dental RF loop coil (**a**) and in-vivo experimental coil set between the upper and lower jaw bite planes in the occlusal position (**b**).

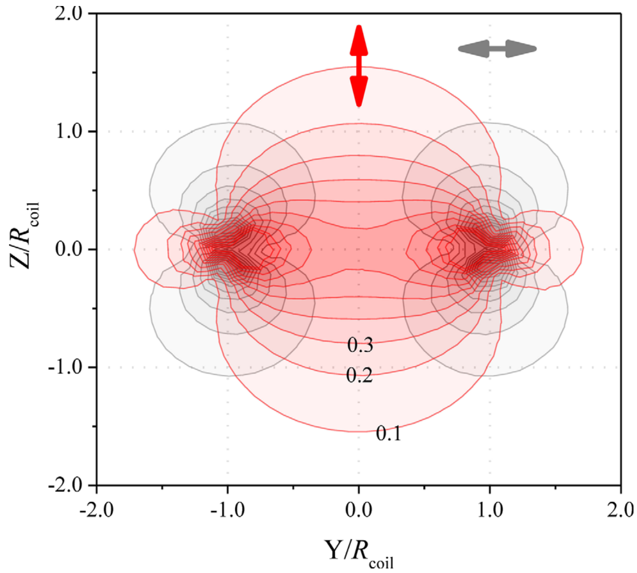

FIG. 2. Intensities of the longitudinal (red) and transverse (black) components of the B_1 field in the YZ plane, as created by a one loop coil of radius R within the XY plane, based on Biot-Savart calculations. Arrows indicate the directions of B_1 field components.

Simulations

The Biot-Savart magnetostatic approximation of the RF field was calculated by using an in-house modified version of the Biot_3d.m program written in Matlab (Copyright © 2011, Sathyanarayan Rao: http://www.mathworks.com/matlabcentral/fileexchange/33409-magnetic-field-of-a-current-loop-using-biot-savarts-law).

Figures 2 and 3a,b present Biot-Savart simulations for one-wire loop coils of radius R centered at (0, 0, 0). To simulate a coil with a wide foil (Fig. 3c), five one-wire loops with appropriate radii, each with the same current, were positioned equidistantly to fill the width of the foil. The longitudinal and transverse components of the B_1 field (defined relative to the coil axis) were calculated. Isocontour lines of the field strength in the YZ plane were calculated, normalized to the maximum value of the longitudinal component, and presented in 10% steps in the same scale. The magnetostatic approximation used in this work does not include the waveguide, dielectric, and skin effects inevitable at high frequencies; however, it is sufficient to allow the presented qualitative discussion and conclusion (please read more in the Discussion section).

MRI Experiments

The phantom and in vivo images were all acquired using a 4 T (90 cm-bore) MRI scanner equipped with a Varian (Agilent) DirectDrive™ console. The available ramp time and field gradient strengths were 0.5 ms and 50 mT/m, respectively.

The phantom used was a 150 mm diameter glass cylinder loaded with tap water. The coil was isolated electrically by using a plastic bag, and then immersed in the water and fixed to the edges of the cylinder. The orientation of the entire cylinder (including the coil) was changed in order to obtain the longitudinal and transverse components at identical load conditions.

The in vivo images were obtained from a normal adult volunteer with the intraoral RF loop coil in the occlusal position. The coil was isolated from intraoral structures, and saliva, by being inserted within a MPTFE bag (Welch Fluorocarbon) of 0.06 × 127 × 102 mm size. The patient lay in supine position with head in a holder specifically designed for restriction of head motion and fixation of the RF coil (Fig. 1b). All in vivo experiments were performed with approval from our university's Institutional Review Board.

For imaging, the SWIFT sequence (18) was used (http://www.cmrr.umn.edu/swift/). Acquisition parameters for the phantom experiment were as follows: $b_w = 104$ kHz, TR = 3.1 ms, number of projections = 32,000, FOV = 22^3 cm^3, and total acquisition time = 110 s. Parameters for the in vivo experiment were as follows: $b_w = 125$ kHz, TR = 2.65 ms, number of projections = 131,000, FOV = 12^3 cm^3, and total acquisition time = 4.5 min. The general parameters: nominal flip angle = 8°, with acquisition of 128 complex points during a gapped HS2 pulse (32,33) and continuous acquisition

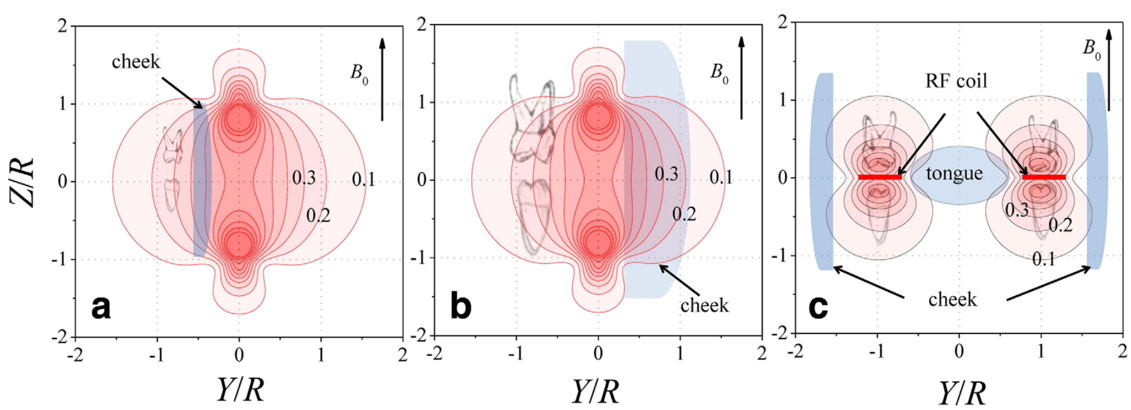

FIG. 3. Schematic of MR effective components of B_1 and objects of interest for dental imaging with conventional coil orientation (coil plan parallel to B_0) in extraoral position ($R = 80$ mm; **a**); conventional intraoral position ($R = 15$ mm; **b**); and with coil in occlusal position ($R = 25$ mm, coil plan orthogonal to B_0; **c**), based on Biot-Savart calculations.

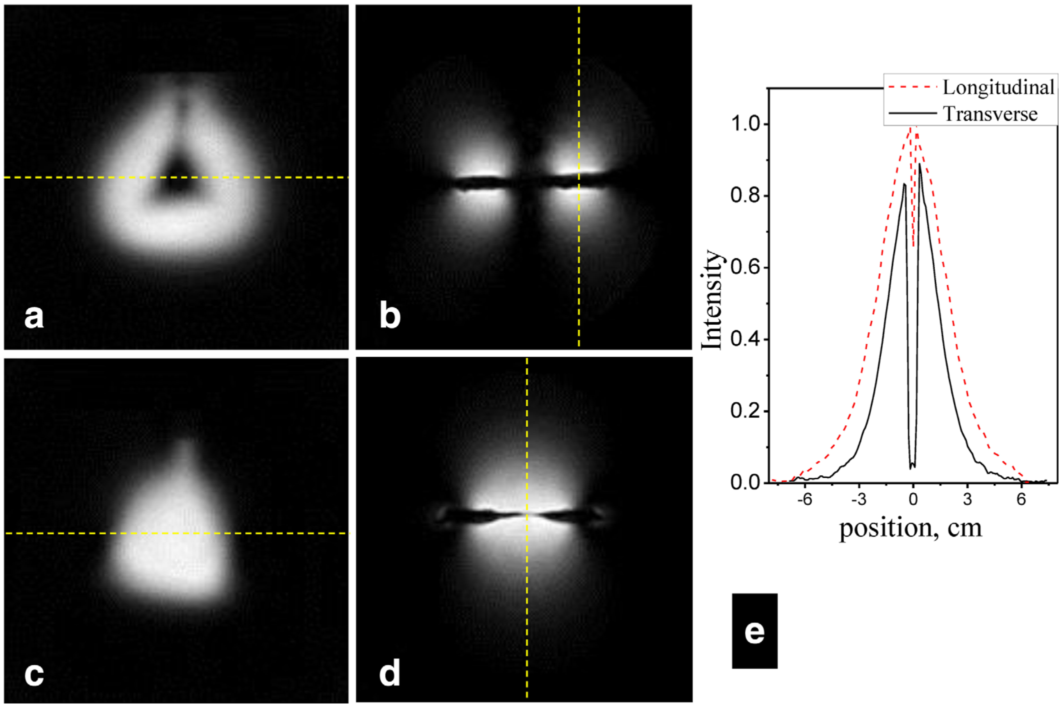

FIG. 4. Selected 3D SWIFT images of the phantom obtained with coil loop plane oriented orthogonally to B_0 (**a**, **b**) and parallel to B_0 (**c**, **d**). Image plane parallel to coil plane (a, c) and orthogonal to the coil plane (b, d). The dotted lines in (a, c) indicate the position of slices in (b, d). The dotted lines in (b, d) indicate the position of intensity profiles plotted at (**e**).

of 128 complex points after the pulse. The time delay between the end of acquiring one projection and the start of the next was fixed at 0.6 ms. The field gradients changed values at the beginning of that delay. Each spoke acquisition results in one center-out line of k-space after pre-processing (radial center-out k-space trajectory). The terminus of the radial spokes grouped in 128 interleaved spirals and acquired with Halton view order (34) forms isotropically distributed points on a sphere. 3D radial SWIFT data were processed using an in-house program developed in LabVIEW (National Instruments) and interpolated with a Kaiser-Bessel function onto a Cartesian grid utilizing in-house MATLAB (Mathworks) mex code to a matrix of 384^3 (yielding 0.3 mm nominal resolution for in vivo experiment). The panoramic slices were created by using the "straighten" plugin (35) in ImageJ, which is a Java based image processing program (36).

RESULTS

Figure 2 presents the calculated isocontour lines of the longitudinal and transverse components of the B_1 field in the YZ plane created by a single-loop surface coil located in the XY plane. In the XY plane and parallel planes, the isocontour lines are radially symmetric, tracing out circles (not shown). Viewed in the YZ plane the contours have differing symmetry for the two orthogonal components. The longitudinal component describes a mirrored shape for each contour, with XY plane of symmetry. The transverse components are presented as two circular shapes (also mirrored) at the position of each crossing of the coil element of the YZ plane. They can be described as two toroidal volumes or "doughnuts" of sensitivity above and below the XY coil loop plane. The longitudinal component has higher values at the center of the coil (and Z axis) relative to the transverse component, and overall has about 10% deeper penetration (measured from the Y plane) relative to transverse component. For excitation and detection in MRI either the longitudinal or transverse components (or combination) of the surface coil B_1 can be used, and this depends only on the orientation of the coil plane relative to Zeeman field, B_0.

Figure 3 schematically shows the field profiles and relative sizes of molar teeth to estimate the relative efficiency of the different approaches using longitudinal components extraorally (Fig. 3a) and intraorally (Fig. 3b), as well as the intraoral approach using transverse components (Fig. 3c).

Figure 4 presents the results of a phantom experiment that compares the sensitive volumes achieved with the coil oriented in the two different orthogonal positions. The experiment was done in exactly the same surrounding media and with the same coil loading, but with rotation by 90°. The expected noise contribution is the same in both cases. For the small flip angle used, the intensity profiles in Figure 4e provide a measure of the B1 distributions and/or SNR. The absolute intensity profiles plotted for these different coil orientations are within about 10 % of each other (Fig. 4e). All of these results match well with the simulated data. 3D in vivo images with the coil loop plane in the occlusal position (using the transverse B_1 field components relative to the coil loop plane) are shown in Figure 5. As was predicted, the teeth and jaw bones are nicely positioned within the sensitive volume of the coil, while the signal from cheek and tongue appear with low intensity.

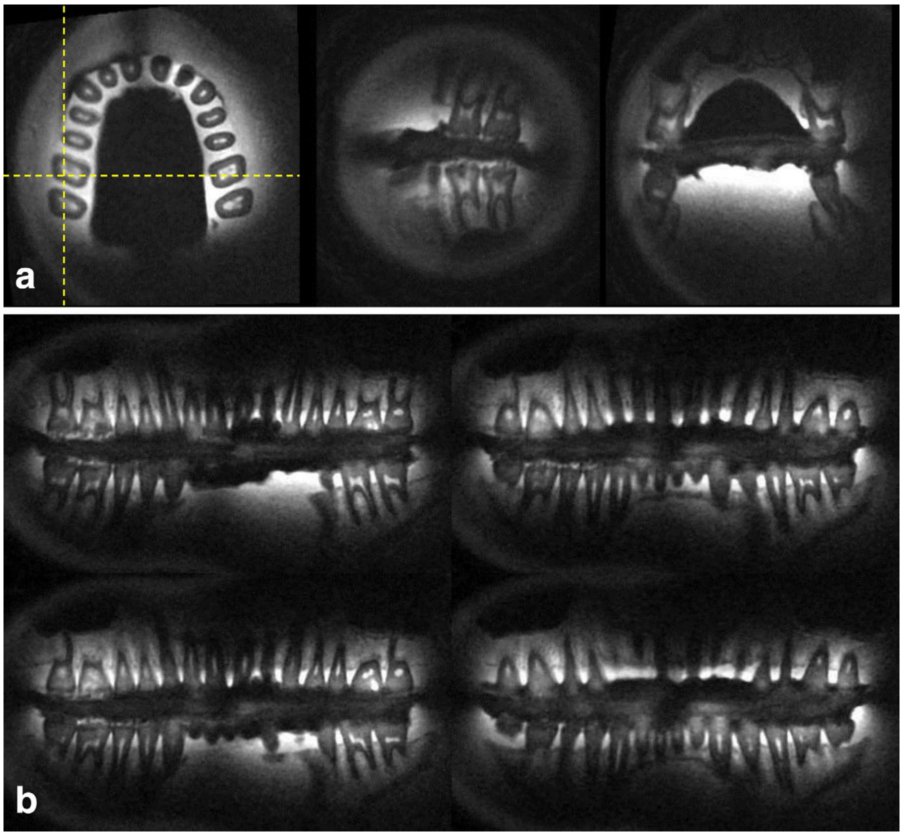

FIG. 5. Three selected orthogonal slices (**a**) and selected panoramic slices (**b**) of a 3D SWIFT image obtained using the transverse components of the B_1 field.

DISCUSSION

Traditionally the plane of an MRI surface coil loop is oriented parallel to B_0 to exploit the longitudinal component of B_1 with extraoral or intraoral positioning, as schematically presented in Figure 3a,b, respectively. The main advantage of extraoral positioning (Fig. 3a) is patient comfort, while disadvantages include low filling factor, low resolution, and the included (noninformative) high amplitude signal from the cheek located next to the coil (29). With intraoral positioning (Fig. 3b), SNR is high and the cheek signal is still high, but can be shielded out (19). However, a main disadvantage could be lower SNR at the position of the tips of teeth.

As was shown with these preliminary images (Fig. 5) dental structures can effectively be covered using the transverse components of B_1 (relative to the loop plane) produced by a single loop coil in the shape of the human arch. The sensitive volume of this coil configuration in the occlusal position includes the most important dental structures, including the teeth and jaws, and excludes large portions of the cheeks, lips, and tongue, which usually have less informative but very intense confounding signals.

The teeth and supporting structures of the dental arches are within the two sensitive toroidal volumes or “doughnuts,” while tissues of less interest (e.g., cheeks, lips, and tongue) are not. This has two significant advantages: (i) maximum coil sensitivity corresponds to the regions of most interest (teeth and supporting structures); and (ii) minimum coil sensitivity corresponds to structures that a dentist is not traditionally trained to interpret, such as skull base and brainstem. It is worth noting that factor ii is responsible for minimizing motion artifacts (radial streaking) originating from the intense signals (cheeks, lips, and tongue) that would be included with other coil configurations.

The reduced intensity in the front teeth position, which is noticeable in Figures 4a and 5a is related to the 2 mm gap between the ends of the copper loop. This deficiency could be circumvented by decreasing the gap or even partly overlapping the coil’s ends in a future coil design.

Here, we have used a single channel coil in transmit-receive mode, although this orthogonal coil can also be as a receive-only coil in combination with another transmitting volume coil. At this point is not obvious how the proposed approach could effectively be used with a parallel imaging technique to accelerate teeth imaging. However, for whole mandibular imaging (20), for example, we believe the orthogonal coil in occlusal position could be used in combination with an array of “conventionally designed” extra or intra oral coils for parallel acquisition.

The Biot Savart calculation, despite its simplicity, is in good agreement with our phantom experiments. This is due to the limited diameter of the coil (5 cm), which in this case is about 40 times smaller than the wavelength in vacuum and about 4 times smaller than the wavelength in high-water-content media (37). However, future research will benefit from full-wave electromagnetic field calculations in complicated dental tissues including air, dentin, enamel, teeth supporting tissues, and saliva, especially in the presence of different restorative materials, such as endosseous implants.

To the best of our knowledge, Figure 5b presents the first MRI panoramic images at such high nominal resolution (0.3 mm^3). The actual spatial resolution is lower due to the effects of residual motion and off-resonance blurring, which for radial acquisition could be compensated at the postprocessing stage and are in the scope of future research.

CONCLUSIONS

The transverse components of the B_1 field of a surface coil in the occlusal position can be effectively used for imaging of teeth and associated structures.

REFERENCES

1. Nasel C, Gahleitner A, Breitenseher M, Czerny C, Solar P, Imhof H. Dental MR tomography of the mandible. J Comput Assist Tomogr 1998;22:498–502.
2. Nasel C, Gahleitner A, Breitenseher M, Czerny C, Glaser C, Solar P, Imhof H. Localization of the mandibular neurovascular bundle using dental magnetic resonance imaging. Dentomaxillofac Radiol 1998;27:305–307.
3. Ploder O, Partik B, Rand T, Fock N, Voracek M, Undt G, Baumann A. Reperfusion of autotransplanted teeth–comparison of clinical measurements by means of dental magnetic resonance imaging. Oral Surg Oral Med Oral Pathol Oral Radiol Endod 2001;92:335–340.
4. Kress B, Buhl Y, Anders L, Stippich C, Palm F, Bahren W, Sartor K. Quantitative analysis of MRI signal intensity as a tool for evaluating tooth pulp vitality. Dentomaxillofac Radiol 2004;33:241–244.
5. Kress B, Buhl Y, Hahnel S, Eggers G, Sartor K, Schmitter M. Age- and tooth-related pulp cavity signal intensity changes in healthy teeth: a comparative magnetic resonance imaging analysis. Oral Surg Oral Med Oral Pathol Oral Radiol Endod 2007;103:134–137.
6. Tutton LM, Goddard PR. MRI of the teeth. Br J Radiol 2002;75:552–562.
7. Lee K, Kaneda T, Mori S, Minami M, Motohashi J, Yamashiro M. Magnetic resonance imaging of normal and osteomyelitis in the mandible: assessment of short inversion time inversion recovery sequence. Oral Surg Oral Med Oral Pathol Oral Radiol Endod 2003;96:499–507.
8. Olt S, Jakob PM. Contrast-enhanced dental MRI for visualization of the teeth and jaw. Magn Reson Med 2004;52:174–176.
9. Lockhart PB, Kim S, Lund NL. Magnetic resonance imaging of human teeth. J Endod 1992;18:237–244.
10. Weglarz WP, Tanasiewicz M, Kupka T, Skorka T, Sulek Z, Jasinski A. 3D MR imaging of dental cavities-an in vitro study. Solid State Nucl Magn Reson 2004;25:84–87.
11. Tymofiyeva O, Rottner K, Gareis D, Boldt J, Schmid F, Lopez MA, Richter E-J, Jakob PM. In vivo MRI-based dental impression using an intraoral RF receiver coil. Conc Magn Reson B: Magn Reson Eng 2008;33B:244–251.
12. Ferretti F, Malventi M, Malasoma R. Dental magnetic resonance imaging: study of impacted mandibular third molars. Dentomaxillofac Radiol 2009;38:387–392.
13. Tymofiyeva O, Rottner K, Jakob PM, Richter EJ, Proff P. Three-dimensional localization of impacted teeth using magnetic resonance imaging. Clin Oral Investig 2010;14:169–176.
14. Bergin CJ, Pauly JM, Macovski A. Lung parenchyma: projection reconstruction MR imaging. Radiology 1991;179:777–781.
15. Gatehouse PD, Bydder GM. Magnetic resonance imaging of short T2 components in tissue. Clin Radiol 2003;58:1–19.
16. Boujraf S, Hofmann C, Ulrici J, Hell E, Haller B, Rasche V. Microstructural assessment of dental tissues by quantitative MRI using ultra-short echo times (UTE): initial in-vivo evaluation. In Proceedings of the 17th Annual Meeting of ISMRM, Honolulu, Hawaii, USA, 2009. p. 4518.
17. Bracher A-K, Hofmann C, Bornstedt A, Boujraf S, Hell E, Ulrici J, Spahr A, Haller B, Rasche V. Feasibility of ultra-short echo time (UTE) magnetic resonance imaging for identification of carious lesions. Magn Reson Med 2011;66:538–545.
18. Idiyatullin D, Corum C, Park J-Y, Garwood M. Fast and quiet MRI using a swept radiofrequency. J Magn Reson 2006;181:342–349.
19. Idiyatullin D, Corum C, Moeller S, Prasad H, Garwood M, Nixdorf D. Dental magnetic resonance imaging: making the invisible visible. J Endod 2011;37:745–752.
20. Kendi ATK, Khariwala SS, Zhang J, Idiyatullin DS, Corum CA, Michaeli S, Pambuccian SE, Garwood M, Yueh B. Transformation in mandibular imaging with sweep imaging with fourier transform magnetic resonance imaging. Arch Otolaryngol Head Neck Surg 2011;137:916–919.
21. Garwood M, Idiyatullin D, Corum CA, et al. Capturing signals from fast-relaxing spins with frequency-swept MRI: SWIFT. Encyclopedia of Magnetic Resonance. Hoboken, NJ: Wiley; 2012. doi:10.1002/9780470034590.
emrstm1259.
22. Hafner S. Fast imaging in liquids and solids with the Back-projection Low Angle ShoT (BLAST) technique. Magn Reson Imaging 1994;12:1047–1051.
23. Madio DP, Lowe IJ. Ultra-fast imaging using low flip angles and FIDs. Magn Reson Med 1995;34:525–529.
24. Weiger M, Pruessmann KP, Hennel F. MRI with zero echo time: hard versus sweep pulse excitation. Magn Reson Med 2011;66:379–389.
25. Weiger M, Pruessmann KP, Bracher AK, Kohler S, Lehmann V, Wolfram U, Hennel F, Rasche V. High-resolution ZTE imaging of human teeth. NMR Biomed 2013;42:20120321.
26. Wu Y, Dai G, Ackerman JL, Hrovat MI, Glimcher MJ, Snyder BD, Nazarian A, Chesler DA. Water- and fat-suppressed proton projection MRI (WASPI) of rat femur bone. Magn Reson Med 2007;57:554–567.
27. Grodzki DM, Jakob PM, Heismann B. Ultrashort echo time imaging using pointwise encoding time reduction with radial acquisition (PETRA). Magn Reson Med 2012;67:510–518.
28. Bracher A-K, Hofmann C, Bornstedt A, Hell E, Janke F, Ulrici J, Haller B, Geibel M-A, Rasche V. Ultrashort echo time (UTE) mr imaging for the assessment of caries lesions. Dentomaxillofac Radiol 2013;42:20120321.
29. Idiyatullin D, Corum C, McIntosh A, Moeller S, Garwood M. Direct MRI of Human Teeth by SWIFT. In Proceedings of the 15th Annual Meeting of ISMRM, Berlin, Germany, 2007. p. 383.
30. Alfonsetti M, Clementi V, Iotti S, Placidi G, Lodi R, Barbiroli B, Sotgiu A, Alecci M. Versatile coil design and positioning of transverse-field RF surface coils for clinical 1.5-T MRI applications. MAGMA 2005;18:69–75.
31. Alfonsetti M, Mazza T, Alecci M. Optimization of multi-element transverse field radio frequency surface coils. Meas Sci Technol 2006;17:N53–N59.
32. Tannus A, Garwood M. Improved performance of frequency-swept pulses using offset-independent adiabaticity. J Magn Reson 1996;A 120:133–137.
33. Idiyatullin D, Corum C, Moeller S, Garwood M. Gapped pulses for frequency-swept MRI. J Magn Reson 2008;193:267–273.
34. .Corum C, Babcock A, Idiyatullin D, Styczynski-Snyder AL, Hutter D, Everson L, Nelson M, Garwood M. Sweep Imaging with Fourier Transform (SWIFT) in Breast Cancer. In Proceedings of the 20th Meeting of ISMRM, Melbourne, Australia, 2012. p. 457.
35. Kocsis E, Trus BL, Steer CJ, Bisher ME, Steven AC. Image averaging of flexible fibrous macromolecules: the clathrin triskelion has an elastic proximal segment. J Struct Biol 1991;107:6–14.
36. Collins T. ImageJ for microscopy. Biotechniques 2007;43:25–30.
37. Vaughan JT. Ultra High Field MRI: High-Frequency Coils. Ultra High Field Magnetic Resonance Imaging. Volume 26, Biological Magnetic Resonance. Springer, Denver, Colorado, USA, 2006. p 127–161.